

Uncovering the internal structure of five-fold twinned nanowires through 3D electron diffraction mapping

Xin Fu(付新)

Citation: Chin. Phys. B . 2020, 29(6): 068101 . **doi:** 10.1088/1674-1056/ab8370
Journal homepage: http://cpb.iphy.ac.cn; http://iopscience.iop.org/cpb

What follows is a list of articles you may be interested in

Improved performance of back-gate MoS_2 transistors by NH_3-plasma treating high-*k* gate dielectrics

Jian-Ying Chen(陈建颖), Xin-Yuan Zhao(赵心愿), Lu Liu(刘璐), Jing-Ping Xu(徐静平)
Chin. Phys. B . 2019, 28(12): 128101 . **doi:** 10.1088/1674-1056/ab50fe

Chemical vapor deposition growth of crystal monolayer SnS_2 with NaCl-assistant

Xiao-Xu Liu(刘晓旭), Da-Wei He(何大伟), Jia-Qi He(何家琪), Yong-Sheng Wang(王永生), Ming Fu(富鸣)
Chin. Phys. B . 2019, 28(11): 118101 . **doi:** 10.1088/1674-1056/ab457c

Annealing-enhanced interlayer coupling interaction inGaS/MoS_2 heterojunctions

Xiuqing Meng(孟秀清), Shulin Chen(陈书林), Yunzhang Fang(方允樟), Jianlong Kou(寇建龙)
Chin. Phys. B . 2019, 28(7): 078101 . **doi:** 10.1088/1674-1056/28/7/078101

Formation and stability of ultrasonic generated bulk nanobubbles

Chen-Ran Mo(莫宸冉), Jing Wang(王菁), Zhou Fang(方舟), Li-Min Zhou(周利民), Li-Juan Zhang(张立娟), Jun Hu(胡钧)
Chin. Phys. B . 2018, 27(11): 118104 . **doi:** 10.1088/1674-1056/27/11/118104

Observation of oscillations in the transport for atomic layer MoS_2

Xiao-Qiang Xie(解晓强), Ying-Zi Peng(彭英姿), Qi-Ye Zheng(郑奇烨), Yuan Li(李源), Ji Chen(陈吉)
Chin. Phys. B . 2018, 27(2): 028103 . **doi:** 10.1088/1674-1056/27/2/028103

Uncovering the internal structure of five-fold twinned nanowires through 3D electron diffraction mapping*

Xin Fu(付新)[1,2,3,4,†]

[1] GRINM Group Corporation Limited, National Analysis and Testing Center for Nonferrous Metals and Electronic Materials, Beijing 101400, China
[2] Guobiao (Beijing) Testing & Certification Co., Ltd., Beijing 101400, China
[3] China United Test & Certification Co., Ltd., Beijing 101400, China
[4] General Research Institute for Nonferrous Metals, Beijing 100088, China

(Received 15 January 2020; revised manuscript received 2 March 2020; accepted manuscript online 26 March 2020)

Five-fold twinned nanostructures are intrinsically strained or relaxed by extended defects to satisfy the space-filling requirement. Although both of metallic and semiconductor five-fold twinned nanostructures show inhomogeneity in their cross-sectional strain distribution, the evident strain concentration at twin boundaries in the semiconductor systems has been found in contrast to the metallic systems. Naturally, a problem is raised how the chemical bonding characteristics of various five-fold twinned nanosystems affects their strain-relieving defect structures. Here using three-dimensional (3D) electron diffraction mapping methodology, the intrinsic strain and the strain-relieving defects in a pentagonal Ag nanowire and a star-shaped boron carbide nanowire, both of them have basically equal radial twin-plane width about 30 nm, are non-destructively characterized. The non-uniform strain and defect distribution between the five single crystalline segments are found in both of the five-fold twinned nanowires. Diffraction intensity fine structure analysis for the boron carbide five-fold twinned nanowire indicates the presence of high-density of planar defects which are responsible for the accommodation of the intrinsic angular excess. However, for the Ag five-fold twinned nanowire, the star-disclination strain field is still present, although is partially relieved by the formation of localized stacking fault layers accompanied by partial dislocations. Energetic analysis suggests that the variety in the strain-relaxation ways for the two types of five-fold twinned nanowires could be ascribed to the large difference in shear modulus between the soft noble metal Ag and the superhard covalent compound boron carbide.

Keywords: five-fold twinnining, elastic strain, structural relaxation, electron diffraction mapping

PACS: 81.07.–b **DOI:** 10.1088/1674-1056/ab8370

1. Introduction

Up to now, five-fold twinning has been found in widespread materials including face-centered cubic (FCC) metals (such as Au, Ag, Cu), semiconductors (such as Si, Ge, diamond), covalent compounds, and even organic materials.[1–5] Nanoscale five-fold twinned structures have drawn more research interests for many decades due to their unusual symmetry[1,6] and the unique properties, such as anomalous strength,[7,8] tunable plasmonic properties,[9] and enhanced catalytic activity.[2,10]

Ideally, each of the five equally shaped single crystalline segments composing a five-fold twinned structure encloses an angle of 72°. However, in the known five-fold twinned structures an intrinsic angular misfit remains due to the incomplete 360° space-filling. For FCC metals or diamond-cubic materials, the dihedral angle between {111} twin planes is 70.35° which results in a well-known angular deficiency of 7.35° in the formation of five-fold twinning.[1] Superhard α-rhombohedral boron suboxide (B_6O) nearly fits the space-filling requirement of five-fold twinning by remaining an angular deficiency about 1°.[5] But α-rhombohedral boron carbide (nominal atomic content B_4C, space group $R\bar{3}m$) five-fold twinned structures have been found to accommodate an angular excess in the range from 4.55° to 5.25°.[4] Due to the geometric incompatibility in the formation of five-fold twinning, both of the earlier theoretical predictions[6,11] and the recently experimental observations[12,13] have proposed the presence of naturally occurring inhomogeneous strain field. Because the elastic strain energy in five-fold twinned structures increases exponentially with the radius,[11] above a critical radius it will be relaxed by extended defects.[6,14,15] Undoubtedly, uncovering the internal strain and the defect structures of five-fold twinned nanostructures is mostly important for understanding and controlling their properties.

Recently, aberration-corrected electron microscopy investigation combined with first-principles simulation has indicated that semiconductor (diamond, silicon) five-fold twinned structures exhibit shear-modulus-dependent strain concentration at twin boundaries in contrast to the relatively smooth strain distribution in metallic five-fold twinned structures.[3] But it has been unclear how the chemical bonding characteristics influence the structural relaxation phenomena in five-fold

*Project supported by the National Natural Science Foundation of China (Grant Nos. 51201015 and U1532262).
†Corresponding author. E-mail: fuxints@126.com
© 2020 Chinese Physical Society and IOP Publishing Ltd

twinned nanostructures and the related mechanism should be explored both experimentally and theoretically. Until now, the experimental studies on the strain-relaxation phenomena and the related mechanism of five-fold twinned structures were almost focus on the metallic objects.[15–20] In comparison, limited experimental investigations revealed the defect structures for the elastic strain relaxation in covalent five-fold twinned structures.[14,21–24]

In this work, the strain-relieving defects have been non-destructively revealed in two types of five-fold twinned nanowires (FTNWs) using 3D electron diffraction mapping methodology. One is a pentagonal Ag nanowire with diameter of 55 nm and the other is a star-shaped B_4C nanowire with diameter of 92 nm, both of them have basically equal twin-plane width in the radial direction. The 3D electron diffraction mapping methodology allows to obtain the 3D intensity distribution of specific reflections diffracted from nanostructures[18,21] in a relatively small tilting range compared with real-space electron tomography.[25] Traditionally, the transverse structural observation of one-dimensional (1D) nanostructures in transmission electron microscope (TEM) required the cross-sectional sample preparation which inevitably introduces external strain or defects interfering the characterization of the intrinsic structures. In comparison, 3D electron diffraction mapping has shown a non-destructive nature in the characterization of cross-sectional strain and defects of 1D nanostructures.[18,21] By using this methodology, the non-uniform strain and defect distribution between the five single crystalline segments in two FTNWs have been found. For the 55-nm-diametered Ag nanowire, the inhomogeneous strain is partially relieved by introducing stacking fault layers accompanied by partially dislocations localized near the twin boundaries or in the middle of the single crystalline segments. In contrast, the internal strain in the 92-nm-diametered B_4C nanowire with high shear modulus is almost totally relieved by the formation of high density of planar defects, such as stacking faults and microtwins, in each single crystalline segment. Energetic analysis suggested that the different strain relaxation phenomena in the two types of FTNWs are closely connected with their shear modulus. To understand the related mechanism behind further theoretical investigation by first-principle calculations is required.

2. Materials and method

2.1. Materials

To reveal how the chemical bonding characteristics of various five-fold twinned nanosystems affects their strain-relieving defect structures, two types of FTNWs, metallic and covalent, were selected in the study. It is well known that Ag FTNWs are among the most researched metallic five-fold twinned nanostructures due to their facile synthesis method[26] and the potential applications.[2,8] Thus commercial Ag FTNWs were used for the internal structure characterization in this study. Covalent five-fold twinned nanostructures are widely found in semiconductors (such as Si, Ge, diamond) and compounds. But Si or Ge five-fold twinned nanostructures are mostly formed in semiconductor thin films.[1] Usually, the synthetic Si nanowires have been found to have a single crystalline structure.[27–29] It has been found that α-rhombohedral boron-rich compounds, such as B_6O and B_4C, can form five-fold twinned nanowire structures. However, the angular misfit of B_6O five-fold twinned structures is only about 1°,[5] which is much smaller than the 7.35° angular deficiency in the formation of Ag five-fold twinned structures. The big difference in the misfit angle can cause the difference in strain distribution and the related strain-relieving defect structures between B_6O and Ag FTNWs. In contrast, B_4C FTNWs have show a misfit angle about 5°,[4] which is more comparable to that of the Ag FTNWs. Thus the B_4C FTNWs were chosen for the internal structure comparison study with the Ag FTNWs.

The B_4C FTNWs as shown in Fig. 1(a) were synthesized by solid state sintering at 1100 °C using a pellet made from Fe_3O_4, BaO, and amorphous boron powders.[4] The composition and the crystal structure of the sintered nanowires have been identified by systematic tilting electron diffraction analysis and electron energy loss spectroscopy.[4] The Ag FTNWs as shown in Fig. 1(b) were supplied by Blue Nano Inc. The TEM specimens were prepared by ultrasonic dispersion of the nanowires diluted with ethanol. In this study, we choose a 55-nm-diametered pentagonal Ag nanowire and a 92-nm-diametered star-shaped B_4C nanowire for the internal structure analysis. The five-fold twinning orientation relationships of both of nanowires were confirmed by systematic tilting electron diffraction analysis (see Appendix A: Supporting information, Fig. A1 and Fig. A2). Although the two types of FTNWs have different diameters, they have basically equal radial twin-plane width about 30 nm which is directly concerning with the analysis and comparison about the internal elastic strain and the related strain-relieving defect configuration (in Section 4).

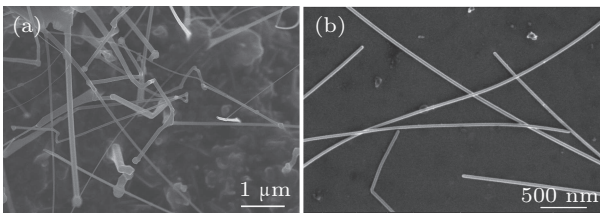


Fig. 1. Scanning electron microscope (SEM) images of (a) the sintered B_4C nanowires and (b) the solution-synthesized Ag nanowires dispersed on a silicon wafer.

The α-rhombohedral B_4C nanowires synthesized in a solid-state reaction at 1100 °C have shown a star-shaped or

truncated star-shaped cross-sectional morphology in scanning electron microscope (SEM).[4] The electron diffraction analysis for the B_4C FTNWs (supporting information Fig. A1) has revealed a cyclic five-fold twinned structure with five crystallites shearing a common [001] (hereafter we use the rhombohedral representation of B_4C unit cell) twinning axis (TA) and being adjacent to each other by {100} twin plane[4,14] as shown in Fig. 2(a). Figure 2(c) demonstrates the atomic structure of B_4C rhombohedral lattice. The carbon-content-dependent lattice parameter of α for B_4C is varying in the range from 65.4 to 65.7°. It results in the dihedral angle between {100}-type planes (as shown in Fig. 2(c), the shadowed (100) and (010) crystallographic planes) ranging from 72.09° to 73.05°.

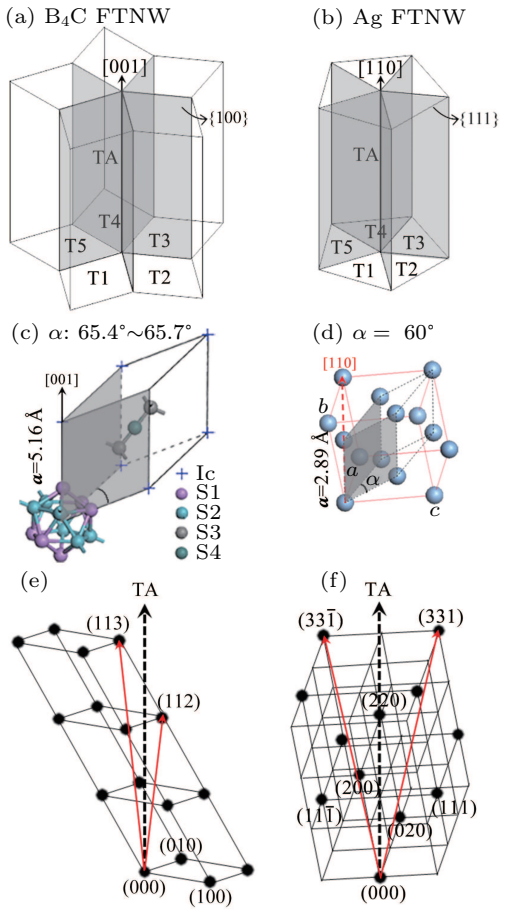


Fig. 2. Panels (a) and (b) demonstrate the ideal structural models of B_4C star-shaped FTNW and Ag pentagonal FTNW, respectively. The black arrow lines indicate the twinning axes (TA) of both of the nanowires. The twin planes of the FTNW structural models are shadowed in panels (a) and (b). (c) The atomic structure of B_4C rhombohedral unit cell. S1, S2, S3, and S4 indicate the four atomic sites in the unit cell. S1 and S2 are at the polar and equatorial sites of the icosahedral clusters, respectively. S3 and S4 are at the end and the center of the linear atomic chain. Ic represents the icosahedral cluster. The carbon content-dependent lattice parameter α varies in the range from 65.4° to 65.7°. To form five-fold twinned structure, the B_4C single crystalline segments share a common [001] twining axis as indicated by black arrow line and join together by (100) and (010) twin planes which are shadowed. (d) The atomic structure of Ag FCC unit cell indicated by red solid lines. The corresponding Ag rhombohedral primitive unit cell is indicated by black dashed lines. Its rhombohedral unit cell parameters are as $a = 2.89$ Å, $\alpha = 60°$. (e) The reciprocal lattice of a B_4C single crystal. (f) The reciprocal lattice of an Ag FCC single crystal.

Therefore, in the formation of B_4C FTNW by joining five single crystalline segments together, an angular excess in the range from 4.55° to 5.25° will be remained.

For Ag FCC lattice, the primitive unit cell is rhombohedral structure as illustrated by black dashed lines in Fig. 2(d). Its rhombohedral lattice parameters are as $a = 2.89$ Å, $\alpha = 60°$. The {111} crystallographic plane of Ag FCC lattice is equivalent to the {100} plane of the rhombohedral lattice. And the ⟨110⟩ direction of Ag FCC lattice is equivalent to the ⟨001⟩ direction of the rhombohedral lattice. In this study, the FCC structure is used for the index of Ag FTNWs. Systematic electron diffraction analysis (supporting information, Fig. A2) has confirmed that the Ag FTNW composes five single crystalline FCC segments joining together by sharing their {111} twin planes which coincide along the ⟨110⟩ twinning axis as shown in Fig. 2(b). According to the Ag FCC structure, the dihedral angle between the adjacent {111} crystallographic planes (the shadowed planes as shown in Fig. 2(d)) is 70.35° which results in the well known angular deficiency of 7.35° (= 360°–70.35° × 5) remained in the formation of FCC five-fold twinned structures.

2.2. Method of 3D electron diffraction mapping

As shown in Fig. 3, the 3D electron diffraction mapping was carried out by tiling the FTNWs along the axis (*i.e.*, tilting axis in Fig. 3(a)) perpendicular to both of the nanowire twinning axis and the incident electron beam with tilting step of 0.2°, meanwhile the series of electron diffraction patterns was recorded by a Gatan 832 CCD camera.[30] To ensure that in a relatively narrow tilting range about ±15°, the scanning reciprocal-space region contains the diffraction contribution from all the single crystalline segments of the examined FTNW, the reflections near around the twinning axis of the examined FTNW have been chosen for the further data process. As shown in Fig. 2(e), the angle of the reciprocal vector, $\boldsymbol{g}_{(112)}$ and $\boldsymbol{g}_{(113)}$, of a single crystalline segment with the twinning axis of the B_4C FTNW (assuming the rhombohedral lattice parameter $\alpha = 65.6°$) is 6.77° and 6.22°, respectively. To enhance the resolution along the Y direction in the reciprocal space [Fig. 3(a)], the (112) reflections of the B_4C FTNW has been chosen for the analysis. For Ag FTNW, the (331) and $(33\bar{1})$ reflections whose corresponding reciprocal vectors (*i.e.*, $\boldsymbol{g}_{(331)}$ or $\boldsymbol{g}_{(33\bar{1})}$) deviated about 13.26° from the [110] twinning axis [Fig. 2(f)] have been used for the analysis. The overall tilting angles for the examined Ag FTNW and the B_4C FTNW were about 30° and 20°, respectively. The experimental raw data of the systematic electron diffraction patterns (see Appendix A: Supporting information, Fig. A3 and Fig. A4) was aligned and mathematically processed by homemade program based on Matlab.[30] For the Ag FTNWs, to

reduce the electron irradiation damage effects the low electron dose rate about 85 e/(nm^2/s) was employed for the 3D electron diffraction mapping. The electron beam dynamic effects on the diffraction intensity reconstruction of B_4C FTNWs[21] and Ag FTNWs[18] have been evaluated. And we believe that they are trivial in this study.

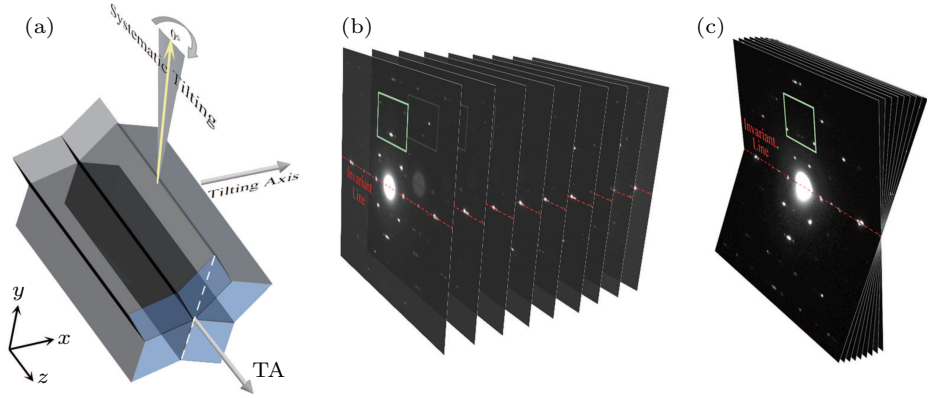


Fig. 3. The schematics of the operation of 3D electron diffraction mapping for FTNWs and the reciprocal-space geometric relationship of the recorded systematic electron diffraction patterns. (a) The geometric relationship between the systematic tilting range and the tilting axis, as well as the twinning axis of an ideal B_4C star-shaped FTNW. Here the origin of the tilting angle (*i.e.*, 0°) is defined as that the incident electron beam is perpendicular to both of the tilting axis and the twinning axis (TA) of the FTNW. At the orientation of the tilting angle equal to 0°, the incident beam is parallel to the mirror-symmetric axis of the cross-section of the FTNW as indicated by the white dashed line. (b) The recorded systematic tilting electron diffractions. These diffraction patterns share a common feature of a set of diffraction spots along an invariant line (indicated by red dashed line) which is parallel to the tilting axis. The green rectangles indicate the data-extracted areas which are used for the post data process of the 3D reconstruction of the diffraction intensity of specific reflections. (c) The geometric relationship of the recorded diffraction patterns in the reciprocal space. For simplicity of the presentation, here we only show nine diffraction patterns in panels (b) and (c).

To precisely identify the orientation relationship between the five single crystalline segments of the FTNWs, two groups of reflections were reconstructed for each FTNW. For the Ag FTNW, the reciprocal volume containing (331) and $(33\bar{1})$ groups was reconstructed. For the B_4C FTNW, the reconstructed reciprocal volume contained (112) and (113) groups. Then the relative orientation relationships between the five $\boldsymbol{g}_{(002)}$ vectors and $\boldsymbol{g}_{(001)}$ vectors were deduced for the Ag FTNW and the B_4C FTNW, respectively. They are directly corresponding to the relative orientation relationships between the five single crystalline segments of both FTNWs. This approach is more precise for the orientation relationship identification of five single crystalline segments of the FTNW than our previous identification method (supporting information, Fig. A3) by locating the center of five equivalent reflections.[18,21]

3. Results

3.1. B_4C FTNW

We carried out 3D electron diffraction mapping for a B_4C FTNW with diameter of 92 nm as shown in Fig. 4(a). Using the series of systematic tilting electron diffraction patterns, the 3D reciprocal data set containing (112) and (113) reflections was reconstructed as shown in Fig. 4(b) in which the intensity-isosurfaces around (112) and (113) diffraction spots are demonstrated. By locating the intensity maximum of each reflection in Fig. 4(b), the diffraction centers of (112) and (113) reflections for T1∼ T5 crystalline segments were identified. For each segment, the vector linking its (112) and (113) diffraction centers is used to define the corresponding reciprocal vector of $\boldsymbol{g}_{(001)}$ as shown in Fig. 4(b) in which only the vector of $\boldsymbol{g}_{(001)}$ for T1 segment is illustrated. For clarity, the five $\boldsymbol{g}_{(001)}$ reciprocal vectors deduced from the 3D data set in Fig. 4(b) for the segments of T1∼ T5, are illustrated in Fig. 4(c). The lengths of the five $\boldsymbol{g}_{(001)}$ reciprocal vectors for T1∼ T5 segments, are 2.28 nm^{-1}, 2.18 nm^{-1}, 2.23 nm^{-1}, 2.25 nm^{-1}, and 2.24 nm^{-1}, respectively. These results are consistent with the theoretical value of 2.22 nm^{-1} calculated according to the parameters of B_4C rhombohedral lattice ($a = 5.17$ Å, $\alpha = 65.52°$). In addition, the angle between the adjacent $\boldsymbol{g}_{(001)}$ reciprocal vectors are calculated to be 29.4°, 28.0°, 33.0°, 32.4°, and 29.7°, respectively, as illustrated in Fig. 4(c). Furthermore, the projections of the five $\boldsymbol{g}_{(001)}$ vectors on the plane perpendicular to the twinning axis of the B_4C FTNW are demonstrated in Fig. 4(d) which indicates a large discrepancy about 10° in the intersection angles between the adjacent projected vectors. These evident angular deviations exhibited in Figs. 4(c) and 4(d) imply a non-uniform structural relaxation in this B_4C FTNW.

As the intensity distributions of specific reflections diffracted from a finite nano-sized crystallite are strongly affected by the nano-object shape, internal strain and defects, to uncover the cross-sectional morphology, relaxation mechanism and the related defect structures of the B_4C FTNW, the 2D intensity distribution of (112) reflections in the reciprocal plane perpendicular to the nanowire twinning axis is extracted from the 3D data set shown in Fig. 4(b). The result is shown in Fig. 5(a). The different flare features around the five (112) diffraction centers further indicate the inhomogeneous structural relaxation within the five crystallites of the B_4C FTNW.

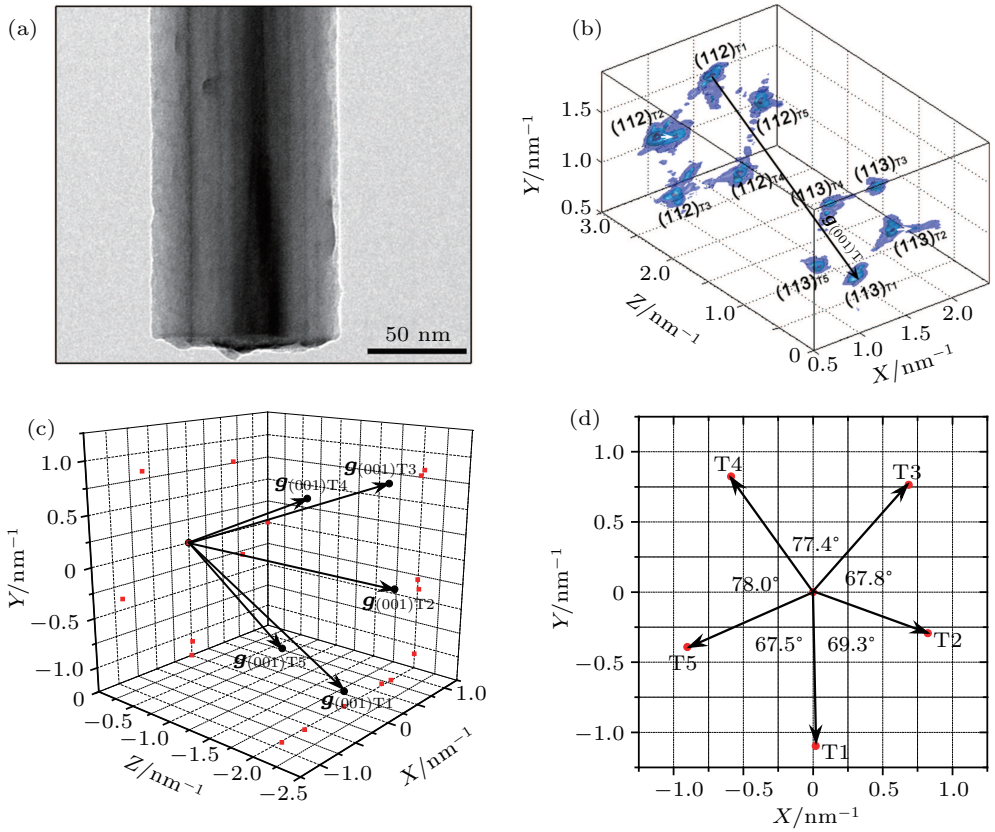


Fig. 4. (a) TEM bright field morphology of a B_4C FTNW with diameter of 92 nm. (b) 3D intensity reconstruction about (112) and (113) reflections of the B_4C FTNW shown in panel (a). In this 3D data set, the direction, Z, is parallel to the twinning axis of the B_4C FTNW, and the direction, X, is parallel to the tilting axis for conducting the systematic tilting electron diffraction. According to the 3D reconstruction result shown in panel (b), the $\boldsymbol{g}_{(001)}$ recirprocal vectors of the five single crystalline segments, T1∼ T5, are deduced and illustrated by black solid lines with arrows in panel (c). In panel (c), the red dots represent the ending points of $\boldsymbol{g}_{(001)}$ vectors projected on X–Y, X–Z, and Y–Z reciprocal planes, respectively. (d) The projections of the five $\boldsymbol{g}_{(001)}$ vectors on the X–Y reciprocal plane which is perpendicular to the twinning axis of the nanowire, *i.e.*, Z direction.

As demonstrated in Fig. 5(a), the flare of $(112)_{T5}$ shows regular spaced ripples along the direction indicated by the white dotted line AB which is perpendicular to the twin plane between T4 and T5 segments. The kinematic simulation of electron diffraction pattern[21] has indicated that this intensity feature could be attributed to the cross-sectional shape effect of single crystalline segment with surface bounded by {100} planes as the ideal structural model shown in Fig. 2(a). The intensity profile along the AB line shown in Fig. 5(b) demonstrates the spacing of the ripples is approximately 0.05 nm^{-1} which reflects the real space distance about 20 nm between the twin plane and its parallel {100} surface of T5 segment. Accordingly, assuming that this B_4C FTNW with five equally sized segments, we can deduce the nanowire diameter about 64 nm. However, the bright field image of the nanowire as shown in Fig. 4(a) indicates that the diameter of the nanowire is 92 nm. Thus it suggests that for this B_4C FTWN, the five crystallites have different cross-sectional sizes or morphologies. Actually, both of the theoretical prediction about the structural relaxation mechanism of five-fold twinned structures[6] and the experimental observation of boron-rich[31] or noble metal five-fold twinned nanowires[6,16] indicate the possibility of the shift of twinning axis towards the periphery and the formation of irregular cross-section. In contrast to the regular spaced ripples, the intensity profile of $(112)_{T5}$ reflection along the line CD which is perpendicular to the twin plane between T1 and T5 segments [Fig. 5(a)] exhibits a streaking. As shown in Fig. 5(b), the full width at half maximum (FWHM) of CD intensity profile is about 0.1 nm^{-1}, which is approximately the 1.5 times wider than that of AB intensity profile. The streaking also exhibits in the intensity profile along the line linking $(112)_{T3}$ and $(112)_{T4}$, as shown in Fig. 5(c). In Fig. 5(c), the FWHM of the $(112)_{T3}$, $(112)_{T4}$ reflection peaks can be measured to be 0.11 nm^{-1}, 0.10 nm^{-1}, respectively. The feature of the flare streaking (*i.e.*, peak broadening in the intensity curves) as shown in Figs. 5(b) and 5(c) indicates the presence of irregular spaced planar defects, such as stacking faults (SFs) or microtwins (MTs). This result is confirmed by the high-resolution TEM image recorded at [010] zone-axis of T4 segment as shown in Fig. 6. Additionally, regular spaced planar defects can also be expected present in T1 and T2 segments. As shown in Fig. 5(c), the intensity profile between the $(112)_{T1}$ and $(112)_{T2}$ diffraction peaks shows an oscillation with periodicity approximately 0.11 nm^{-1} which implies the planar defects with regular spacing about 10 nm.

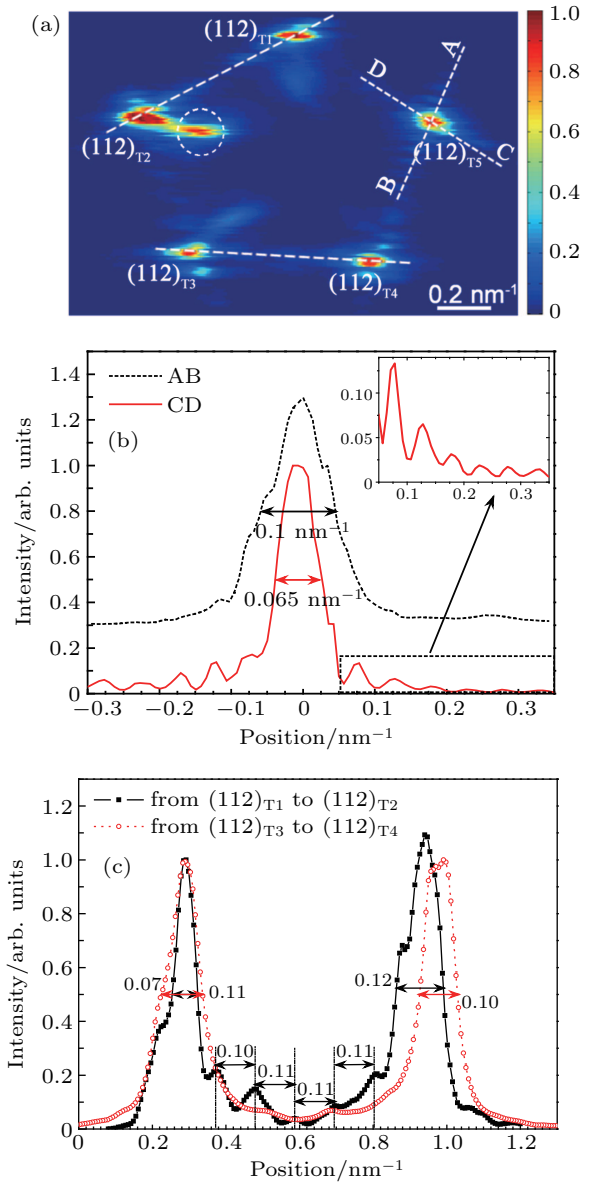


Fig. 5. (a) The 2D intensity distribution in the plane which is perpendicular to the twinning axis of the B_4C FTNW and passes through the five (112) diffraction centers shown in Fig. 4(b). (b) The intensity profiles along the AB and CD lines indicated by white dotted lines in panel (a). For comparison, the CD line profile is vertically shifted as shown in panel (b). (c) The intensity profiles along the white dashed lines across the (112) diffraction peaks of T1 and T2, as well as that of T3 and T4, as shown in panel (a).

In Fig. 5(a), it should be noted that an abnormal strong flare next to the $(112)_{T2}$ reflection as indicated by dashed circle. The intensity maximum of the strong flare is comparable with the five (112) diffraction peaks, and cannot be attributed to shape effect, lattice distortion or defects. It is most probably diffracted from a B_4C crystallite attached to the surface of T2 segment with a small misorientation angle. As shown in Fig. 4(b), a strong flare also appears next to the reflection of $(113)_{T2}$ and is deviated from $(113)_{T2}$ reflection center along the direction approximately parallel to that of the $(112)_{T2}$ neighboring flare deviated from the $(112)_{T2}$ reflection center. This also suggests the presence of a crystallite attached to the nanowire surface.

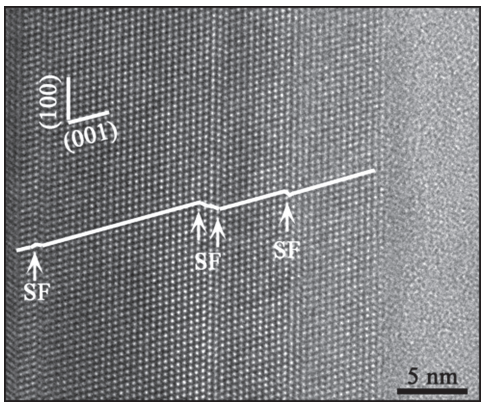


Fig. 6. High-resolution TEM image of T4 segment oriented to [010] zone-axis showing irregular spaced stacking faults (SF).

3.2. Ag FTNW

A Ag FTWN with diameter of 55 nm as shown in Fig. 7(a) was examined through the 3D electron diffraction mapping approach. The 3D intensity distribution of (331) and $(33\bar{1})$ reflections of this nanowire is demonstrated in Fig. 7(b). For each single crystalline segment, the vector starting from the $(33\bar{1})$ diffraction center and ending at the (331) diffraction center is corresponding to the reciprocal vector of $\boldsymbol{g}_{(002)}$. Thus the five $\boldsymbol{g}_{(002)}$ vectors are illustrated in Fig. 7(c). Apparently, they are basically on the same reciprocal plane perpendicular to the nanowire twinning axis, *i.e.*, Z axis as shown in Fig. 7(c). The angles between the adjacent $\boldsymbol{g}_{(002)}$ vectors are measured to be 70.24°, 73.63°, 70.87°, 72.51°, 72.76°, respectively as shown in Fig. 7(d). The angular divergence indicates the uneven internal strain and the related internal structure relaxation between the five single crystalline segments.

To analyze the cross-sectional strain and defects of the Ag FTNW shown in Fig. 7(a), the 2D intensity map about (331) and $(33\bar{1})$ reflections in the plane perpendicular to the nanowire twinning axis is extracted from Fig. 7(b) and demonstrated in Fig. 8(a). The variation in the shape and the intensity between the five (331) flares can be observed. It has been proved by both of coherent x-ray diffraction study[12] and 3D electron diffraction mapping,[18] that the intrinsic 7.35° angular deficiency of Ag FTNWs could result in an inhomogeneous strain field which is consistent with the star-disclination theory proposed by De Wit.[11] According to this theory, to form a five-fold twinned nanostructure, the five single crystalline segments are non-uniformly distorted and the five twin boundaries terminate at a partial disclination named as star-disclination which coincides with the twinning axis. For comparison, we have built a structural model of a 55-nm-diametered Ag FTNW with a star-disclination core along its twinning axis shared by five equal-sized single crystalline segments. According to this model, the 2D intensity map of (331) reflection for each single crystalline segment is calculated

through kinematic electron diffraction simulation. The simulation result is shown in the left bottom corner of Fig. 8(a). Obviously, the pure inhomogeneous star-disclination strain field induces the streaking of (331) reflection toward $\boldsymbol{g}_{(1\bar{1}1)}$ and $\boldsymbol{g}_{(\bar{1}11)}$ directions. For clarity, the intensity line profiles along the $\boldsymbol{g}_{(\bar{1}11)}$ and $\boldsymbol{g}_{(1\bar{1}1)}$ directions as indicated by the white dashed line in Fig. 8(a) are extracted and shown in Figs. 8(b) and 8(c), respectively. The asymmetric broadening of $\boldsymbol{g}_{(\bar{1}11)}$ (or $\boldsymbol{g}_{(1\bar{1}1)}$) line profile for the pure star-disclination model (Dis.) can be observed. This asymmetric feature can be evaluated quantitatively by defining the intensity integration ratio of I_2/I_1, herein I_1 represents the intensity integration in the deviation region from -0.01 nm^{-1} to -0.2 nm^{-1}, and I_2 represents the intensity integration in the deviation region from 0.01 nm^{-1} to 0.2 nm^{-1} for the line-profile curves shown in Figs. 8(b) and 8(c). For the star-disclination model (Dis.) of Ag FTNW with diameter of 55 nm, the calculated intensity ratio of the corresponding $\boldsymbol{g}_{(\bar{1}11)}$ (or $\boldsymbol{g}_{(1\bar{1}1)}$) line-profile is 1.27. For comparison, this simulation result and the experimental counterparts are shown in Figs. 8(d) and 8(e). Only the intensity integration ratios of $\boldsymbol{g}_{(1\bar{1}1)}$ and $\boldsymbol{g}_{(\bar{1}11)}$ line-profiles of T5 segment are consistent with the theoretically expected value about 1.27 for the pure star-disclination model. For the other segments (T1, T2, T3, and T4), the $\boldsymbol{g}_{(1\bar{1}1)}$ and $\boldsymbol{g}_{(\bar{1}11)}$ line-profile curves show an evident discrepancy in the intensity integration ratio. Besides, as shown in Figs. 8(b) and 8(c) the experimental line-profiles exhibit some unexpected features as compared with their simulation counterpart of the pure star-disclination model (Dis.). For example, the $\boldsymbol{g}_{(\bar{1}11)}$ line-profile of T4 basically exhibits a symmetric feature. And the $\boldsymbol{g}_{(1\bar{1}1)}$ line-profile of T3 shows a broadening compared with the simulated line-profile of star-disclination model. Additionally, the $\boldsymbol{g}_{(\bar{1}11)}$ line-profiles of T1 and T2 show a peak splitting. These discrepancies between the theoretical simulation and the experimental results indicate that for the Ag FTNW with diameter of 55 nm, the inhomogeneous star-disclination strain model cannot very well describe the internal structure. The differences between the experimental intensity curves as shown in Figs. 8(b) and 8(c), also implies that for such a Ag FTNW, the intrinsic angular misfit induced inhomogeneous strain could be partially relieved by the introduction of various defect configurations in the single crystalline segments of T1, T2, T3, and T4.

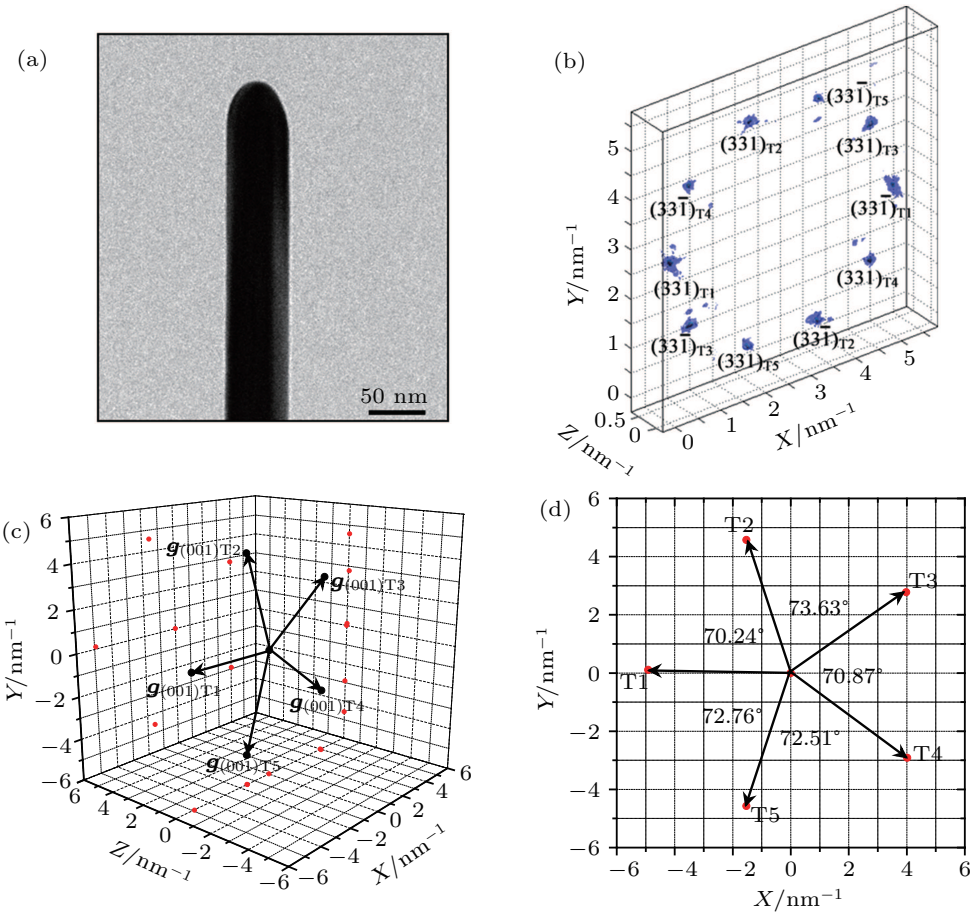


Fig. 7. (a) TEM bright field morphology of a Ag FTNW with diameter of 55 nm. (b) The reconstructed 3D intensity distribution of (331) and $(33\bar{1})$ reflections from the Ag FTNW with diameter of 55 nm as shown in panel (a). (c) The $\boldsymbol{g}_{(002)}$ reciprocal vectors of five single crystalline segments (T1∼ T5) illustrated by black solid lines with arrows and their relative orientation relationship deducted from (b). In panel (c), the red dots represent the ending points of $\boldsymbol{g}_{(002)}$ vectors projected on X–Y, X–Z, and Y–Z reciprocal planes, respectively. (d) The projections of the five $\boldsymbol{g}_{(002)}$ vectors on the X–Y reciprocal plane which is perpendicular to the nanowire twinning axis, *i.e.*, Z direction.

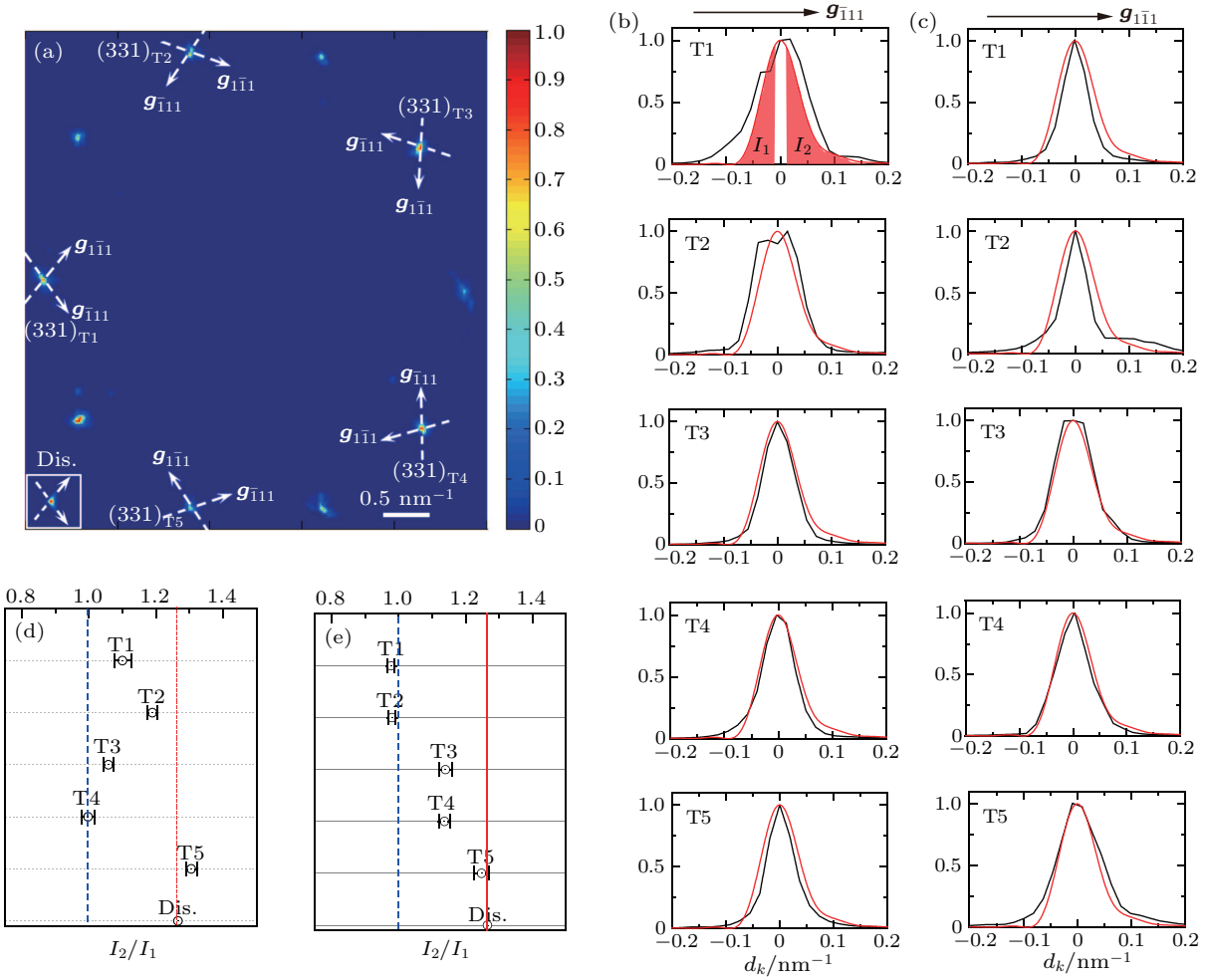


Fig. 8. (a) The 2D intensity distribution of (331) and $(33\bar{1})$ reflections in the plane perpendicular to the twinning axis of the Ag FTNW (*i.e.*, the *Z* axis as shown in Fig. 7(b)). The data are extracted from Fig. 7(b). In the left bottom corner, the kinematic electron diffraction simulation result of (331) reflection is demonstrated. The simulation is based on the pure star-disclination model (Dis.) of a Ag FTNW with diameter of 55 nm. The simulated (331) reflection is oriented as the experimentally reconstructed $(331)_{T1}$ reflection. Panels (b) and (c) show the experimental intensity profiles (black curves) for the T1∼T5 segments compared with the simulated result (red curves) of the pure star-disclination model (Dis.) along the direction of $\boldsymbol{g}_{(\bar{1}11)}$ and $\boldsymbol{g}_{(1\bar{1}1)}$ reciprocal vector, respectively. The experimental line profiles shown in panels (b) and (c) are normalized for comparison with the kinematic simulation result of the pure star-disclination model (Dis.). Panels (d) and (e) illustrate the intensity ratios of I_2/I_1 for the $\boldsymbol{g}_{(\bar{1}11)}$ and $\boldsymbol{g}_{(1\bar{1}1)}$ line-profiles shown in panels (b) and (c), respectively.

For each line-profile shown in Figs. 8(b) and 8(c), with the deviation value approaching 0.15 nm^{-1}, the corresponding diffraction intensity is almost close to the background noise level. This result is in contrast to the counterpart of the B_4C FTNW shown in Figs. 5(b) and 5(c), and implies the significantly less structural defects present in the Ag FTNW with diameter of 55 nm compared with the B_4C FTNW with diameter of 92 nm. The previous studies have confirmed that stacking faults accompanied by partial dislocations are commonly observed in Ag five-fold twinned nanostructures[12,26,32] and these defects are believed to be closely connected with the elastic strain relaxation in five-fold twinned structures.[6] For the Ag nanowires used in this study, the cross-sectional samples were prepared by focused ion beams (FIB). High-resolution TEM observation of these cross-sectional samples indicates the presence of stacking fault layers in the Ag FTNWs. And most single crystalline segments in the observed two Ag FTNW cross-sections contain only one layer of stacking faults (see supporting information, Fig. A6).

To identify the influence of the stacking faults on the intensity distribution of (331) reflections, we carried out a series of kinematic diffraction simulations according to the structural model of Ag single crystalline segment with a single layer of stacking fault. The kinematic diffraction simulation results indicate that the stacking fault layers with distance to their parallel twin plane in the range about from 5 nm to 17 nm, could induce evident streaking or peak splitting of (331) reflection along the direction perpendicular to the stacking fault layers (see supporting information, Fig. A7). By comparing the experimental intensity distribution of (331) reflections shown in Figs. 8(a)–8(c) with the kinematic simulation results (supporting information, Fig. A7), it suggests that in T1 and T2 segments, there possibly exist stacking fault layers which are placed from the twin plane about 16 nm (see supporting information, Fig. A8). But for the segments of T3 and T4, the stacking fault layers most possibly localized

near the twin planes, because that their (331) intensity distributions do not shown evident difference from the simulated result of the pure star-disclination model as shown in Fig. 8(b). Although the stacking fault layers near the corner bonded by {111} twin plane and {100} surface also slightly disturb the (331) reflection intensity distribution (supporting information, Fig. A7), the contribution of such stacking fault configuration to the elastic strain relaxation is less than that of the stacking fault layers localized near the twin plane where the strain is concentrated.[13,33] In addition, high-resolution TEM observation of cross-sectional samples of the Ag FTNWs also supports the common occurrence of stacking fault layers near the twin boundaries.

4. Discussion

Through the analysis of the intensity mapping results of B_4C FTNW with diameter of 92 nm and Ag FTNW with diameter of 55 nm, it can be confirmed that for both of the FTNWs, the star-disclintion-core induced elastic strain could be relieved by introducing defect structures. For the B_4C FTNW with diameter of 92 nm, the evident flares of (112) reflections along the direction perpendicular to the twin planes indicate the presence of high density of planar defects (such as stacking fault and micro-twin) in each single crystalline segment. The elastic strain energy is diminished through the formation of the high density of planar defects in the 92-nm-diametered B_4C FTNW. However, for the Ag FTNW with diameter of 55 nm, the combination of the intensity fine structure analysis and the kinematic electron diffraction simulation indicates that the star-disclination induced elastic strain in some segments (T1, T2, T3, and T4) could be partially relieved by the formation of stacking fault layers accompanied by partial dislocations near the twin plane, or in the middle of the single crystalline segments.

In this study, the two types of FTNWs have different cross-sectional morphology. As shown in Fig. 9, Ag FTNWs have pentagonal cross-section, but B_4C FTNWs have star-shaped cross-section. For the ideal case assuming that the FTNWs have no angular misfit, the diameter of the pentagonal nanowire and the star-shaped nanowire viewing along the mirror symmetric orientation is $1.902R$ and $3.078R$, respectively, here R represents the radial width of the twin planes for the ideal structural models [Fig. 9]. Therefore according to the measured diameters in the bright field images of the Ag FTNW (55 nm, Fig. 7(a)) and B_4C FTNW (92 nm, Fig. 4(a)), their corresponding radial widths of the twin planes are approximately evaluated to be about 29 nm and 30 nm, respectively. Naturally, one problem is posed why such two types of FTNWs have basically equal radial twin-plane width, but exhibit different structural relaxation phenomena. Energetically, the structural relaxation in the five-fold twinned structures arises from the systematic energy minimization which concerning the balance between the accumulative elastic strain energy induced by inhomogeneous lattice distortion and the formation energy of the defect structures.

For FCC five-fold twinned nanostructures, such as Ag FTNWs, there exists an intrinsic angular deficiency (Θ) of 7.35° to be accommodated as shown in Fig. 9(b). However, for α-rhombohedral B_4C, the lattice parameter α is ranging from about 65.4° to 65.7° due to the various carbon content.[4] Therefore, the angular excess (Θ) for B_4C FTNW is in the range from 4.55° to 5.25° [Fig. 9(a)]. To compensate the angular misfit for the five-fold twinned nanostructures, the inhomogeneous strain distribution model named as star-disclination has been theoretically predicted by De Wit earlier in 1970 s,[11] and it has been experimentally confirmed in the past decade.[12,13,18] Supposing that the FTNWs in this study are inhomogeneously strained according to the star-disclination model, the elastic strain energy (in a unit length) induced by the disclination-core could be approximately evaluated as $G\Theta^2R^2/16\pi(1-\nu)$,[11] here Θ is the characteristic rotation angle of the disclination, ν is the Poisson's ratio, G is the shear modulus, and R is the radius of the nanowire by assuming that the nanowires is a long isotropic cylinder.

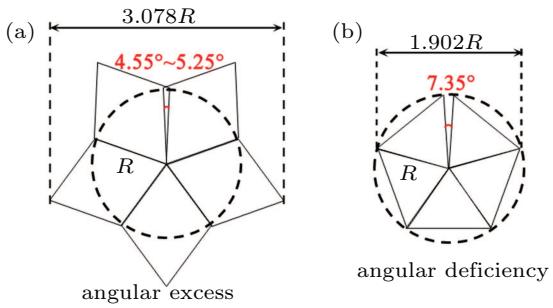


Fig. 9. Cross-sectional geometry of (a) B_4C FTNW and (b) Ag FTNW free of internal strain and defects.

For the Ag FTNW with radius about 30 nm, the reported experimentally measured Poisson's ratio is 0.191 ($\nu = 0.191$).[34] The experimentally measured average Young's modulus (E) for Ag FTNW with diameter about 55 nm is 120 GPa,[8] then we can approximately evaluate the shear modulus for such Ag FTWN to be about 50 GPa according to the relationship $G = E/2(1+\nu)$. Thus we approximately estimate the elastic strain energy (in a unit length) of the Ag star-disclination cylinder with radius of 29 nm to be about 1.7×10^{-8} J/m ($R = 29$ nm, $G = 50$ GPa, $\Theta = 7.35°$, $\nu = 0.191$). Therefore, as shown in Fig. 10, the star-disclination core induced elastic strain energy for the Ag pentagonal FTNW with radial twin-plane width of 29 nm must be less than 1.7×10^{-8} J/m.

Similarly, we can estimate the magnitude of the elastic strain energy (in a unit length) of B_4C FTNW with radius of 30 nm. Because there is not reported experimental result about the Poisson's ratio of B_4C nanowires, we use the value $\nu = 0.18$ for B_4C bulk material[35] as an approximation. The

reported experimentally measured Young's modulus of B_4C nanowires is 428 GPa,[36] then the approximate shear modulus for B_4C nanowire is about 181 GPa according to the relationship $G = E/2(1+\nu)$. Due to the angular misfit (Θ) for B_4C FTNWs in the range from 4.55° to 5.25°, the estimated elastic strain energy (in a unit length) of B_4C FTNW with radius of 30 nm is in the range from 2.5×10^{-8} J/m to 3.3×10^{-8} J/m. Taking account of the star-shaped cross-section morphology of the B_4C FTNW in this study, its corresponding theoretical elastic strain energy (in a unit length) could be larger than the above estimated lower limit of 2.5×10^{-8} J/m, because that the estimation according to the star-disclination model is only considering the inner cylinder part with radius of 30 nm as illustrated in Fig. 10.

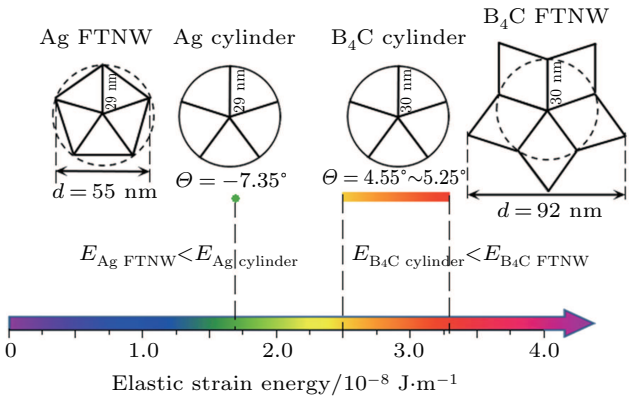


Fig. 10. The calculated elastic strain energies of different FTNW models with star-disclination core.

The angular-misfit induced elastic strain energy is the driving force for the structural relaxation of five-fold twinned nanostructures. The above energetic analysis indicates that the elastic strain energy for B_4C FTNW with diameter of 92 nm is more than 1.5 times larger than that of the Ag FTNW with diameter of 55 nm. Thus in an energetic view, the accumulated elastic strain energy of the 92-nm-diametered B_4C FTNW is prone to be relieved compared with that of the 55-nm-diametered Ag FTNW. According to the theoretical equation for the evaluation of disclination induced elastic strain energy, $G\Theta^2R^2/16\pi(1-\nu)$,[11] even with the same radius, the star-disclination induced elastic strain energy of B_4C FTNW ($G = 181$ GPa, $\nu = 0.18$, $\Theta = 4.55° \sim 5.25°$) is about 30% $\sim$ 80% larger than that of the Ag FTNW ($G = 50$ GPa, $\nu = 0.191$, $\Theta = 7.35°$). Due to the larger shear modulus ($G = 181$ GPa) of B_4C nanowires, the elastic strain energy of B_4C FTNWs increases with the nanowire radius more rapidly than that of Ag FTNWs.

Stacking faults are of common occurrence in Ag FTNWs[1,6,12,26,32] and B_4C FTNWs,[14,21,37] due to their low stacking fault energy. The stacking fault energy of B_4C has been reported to be 75 mJ/m^2.[38] Ag metals have lower stacking fault energy. The earlier experimental publication about Ag stacking fault energy is 22 mJ/m^2,[39] which is larger than the theoretical result predicted by molecular dynamics simulation.[40] But to our knowledge, there are no reported results about Ag five-fold twinned structures with high density of planar defects. The reported cross-sectional TEM observation of thin Ag FTNWs with diameter less than 100 nm indicated that their internal defects, such as partial dislocations and stacking faults, are mostly localized near the twin boundaries.[12,17,26,41,42] This is consistent with our experimental analysis results of 3D intensity mapping and cross-sectional high-resolution observation for the Ag FTNWs with diameter of several tens nanometers. As the Ag FTNWs are growing thicker than few micrometers, the elastic strain could be relieved by opening gaps on one side of the nanowire side faces.[15] Thus we believe that for Ag five-fold twinned structures, the formation of high density of planar defects is not a preferential way to compensate the intrinsic angular deficiency. The disclination induced lattice distortion combined with stacking fault layers and partial dislocations is one of the favorable way for the angular misfit accommodation in Ag FTNWs with diameter less than 100 nm.

Because of the superhard nature for covalent compound B_4C, the presence of partial disclination in B_4C FTNWs could induce higher internal strain. Thus the disclination strain field can only exist in the nanometer-sized core of B_4C FTNWs.[14] For the B_4C FTNW with diameter of 92 nm, the high density of planar defects is the channel for the disclination strain relaxation. In addition, the reported finite element analysis has indicated that the formation of re-entrant surfaces for the five-fold twinned nanostructures can also relieve the elastic strain energy due to the disclination.[43] Therefore, the star-shaped cross-section morphology with five re-entrant groves of the B_4C FTNWs is also ascribed to the elimination of the elastic strain energy.

The above analysis about the intensity fine structure of the B_4C FTNW has indicated the different cross-sectional size of the five single crystalline segments. This can also be confirmed by the peak intensity variation of the five (112) reflections. As shown in Fig. 5(a), the peak intensity of (112) reflection of T2 segment is obviously stronger than that of the other four (112) reflections. Likely, the five (331) reflections of the Ag FTNW also show the difference in the peak value [Fig. 8(a)]. Thus, we believe that for both of the B_4C FTNW and the Ag FTNW in this study, the different cross-sectional sizes of the five single crystalline segments could induce the twinning-axis shift towards the nanowire periphery which is also the way for the elastic strain relaxation.

5. Conclusion

We have carried out 3D electron diffraction mapping for a 92-nm-diametered star-shaped B_4C FTNW and a 55-nm-diametered pentagonal Ag FTNW, both of them have similar radial twin-plane width about 30 nm, to investigate their internal structure details. The analysis of the geometric relation-

ship, intensity distributions and fine structures of the reflection spots in the reconstructed reciprocal volume acquired by the 3D electron diffraction mapping, revealed the inhomogeneous nature of both of the FTNWs.

Due to the different lattice structures, B_4C FTNWs and Ag FTNWs demonstrate different angular-misfit natures. Ag FTNWs consisting of five single FCC crystalline segments remain an intrinsic angular deficiency of 7.35°. But for α-rhombohedral B_4C FTNWs, to form 360° space-filling there exists an angular excess in the range from 4.55° to 5.25° according to the various α lattice parameters. The intrinsic angular misfit for the five-fold twinned nanostructures could induce inhomogeneous lattice distortion around the star-disclination core which coincides with the twinning axis. With the increasing radius of five-fold twinned nanostructures, the elastic strain field could be relieved by defect structures.

For the B_4C FTNW with diameter of 92 nm in this study, quantitative analysis of the strong flares of (112) reflections along the directions perpendicular to the twin planes indicated the presence of high density of planar defects (such as stacking faults or microtwins) in five single crystalline segments which is a way for the elastic strain relaxation. In addition, the twining-axis shift due to the different sizes between the five single crystalline segments and the re-entrant grooves in the star-shaped cross-section can also relieve the star-disclination-induced elastic strain in the B_4C FTNW. However, for the pentagonal Ag FTNW with diameter of 55 nm, the elastic strain is partially relieved by the formation of less localized stacking-fault layers accompanied by partial dislocations, as well as the twining-axis shift.

Energetic analysis indicated that the variety of the strain relaxation ways of the two types of FTNWs is ascribed to the difference in chemical bonding characteristics and the related mechanical properties between the soft noble metal Ag and the superhard covalent compound B_4C. Because of the high shear modulus of B_4C FTNWs, the star-disclination-induced elastic strain field can only exist in a few-nanometer-sized core. With the increase of the radius, the fast-increasing elastic strain energy in the B_4C FTNWs must be relieved through introducing low-energy defect structures, such as stacking faults and microtwins, to minimize the system energy. In comparison, Ag FTNWs have lower shear modulus. Our study confirmed that for pentagonal Ag FTNWs with diameter about 55 nm or even more, the inhomogeneous lattice distortion could coexist with localized stacking fault layers and partial dislocations to compensate the intrinsic angular deficiency of 7.35°.

Acknowledgements

Xin F gratefully thanks Prof. Jun Yuan for the useful discussion about the experimental method.

Appendix A. Supporting information

The five-fold twinned structure identification of the B_4C FTNW with diameter 92 nm by electron diffraction analysis is shown in Fig. A1.

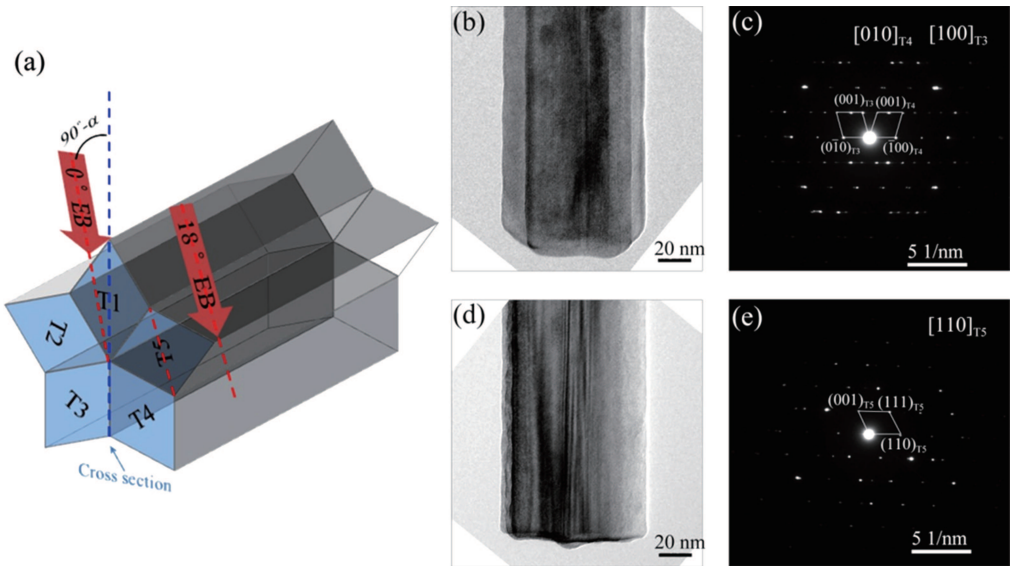


Fig. A1. (a) Schematic view of the relative orientation relationships between the incident electron beam (EB) and the B_4C FTNW. As the incident electron beam parallel to the mirror-symmetric axis of the nanowire cross-section as marked by the blue dashed line which is along the twin boundary between T3 and T4, tilting the nanowire along the direction perpendicular to the twin plane between T3 and T4 segments about 90°-α (α is the lattice parameter of α-rhombohedral B_4C), the twining segments T3 and T4 are oriented to $[100]_{T3}$ and $[010]_{T4}$ zone-axis, respectively. At this orientation (*i.e.*, 0° orientation), the corresponding bright field image and the diffraction pattern are shown in panels (b) and (c), respectively. As the incident electron beam (EB) parallel to the mirror-symmetric axis of the nanowire cross-section indicated by the blue dashed line, rotating the nanowire along its twinning axis about 18° clockwise, the T5 segment is oriented to $[110]_{T5}$ zone-axis. At this orientation (*i.e.*, 18° orientation), the corresponding bright field image and the diffraction pattern are shown in panels (d) and (e), respectively.

The five-fold twinned structure identification of the Ag FTNW with diameter of 55 nm by electron diffraction analysis is shown in Fig. A2.

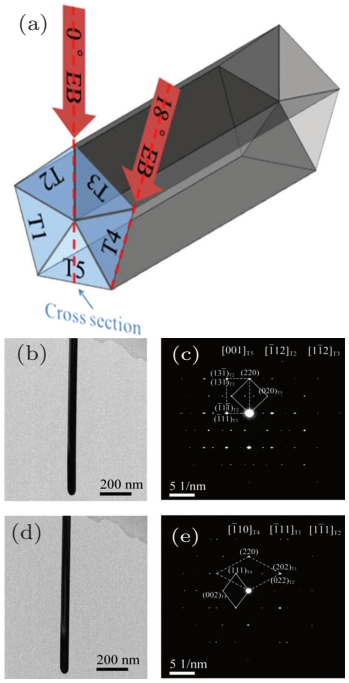


Fig. A2. (a) Schematic view of the relative orientation relationships between the incident electron beam (EB) and the Ag FTNW. As the incident electron beam parallel to the mirror-symmetric axis of the nanowire cross-section which is along the twin boundary between T3 and T4, the twining segments T2, T3, and T5 are oriented to $[\bar{1}12]_{T2}$, $[1\bar{1}2]_{T3}$, and $[001]_{T5}$ zone-axis, respectively. At this orientation (*i.e.*, 0° orientation), the corresponding bright field image and the diffraction pattern are shown in panels (b) and (c), respectively. From the 0° orientation, rotating the nanowire along the twinning axis about 18° counterclockwise, the twinning segments, T1, T2, and T4, are oriented to $[\bar{1}11]_{T1}$, $[1\bar{1}1]_{T2}$, and $[\bar{1}10]_{T4}$ zone-axis, respectively. At this orientation (*i.e.*, 18° orientation), the corresponding bright field image and the diffraction pattern are shown in panels (d) and (e), respectively.

The schematic view of the method of orientation relationship identification by locating the diffraction center of five equivalent reflections of FTNWs is plotted in Fig. A3. This method is suitable for the FTNWs with five single crystalline segments sharing a common twinning axis (*i.e.*, the twinning axis of B_4C FTNW coincides with the [001] crystallographic direction of each single crystalline segment, and the twinning axis of Ag FTNW coincides with the [110] crystallographic direction of each of single crystalline segments.

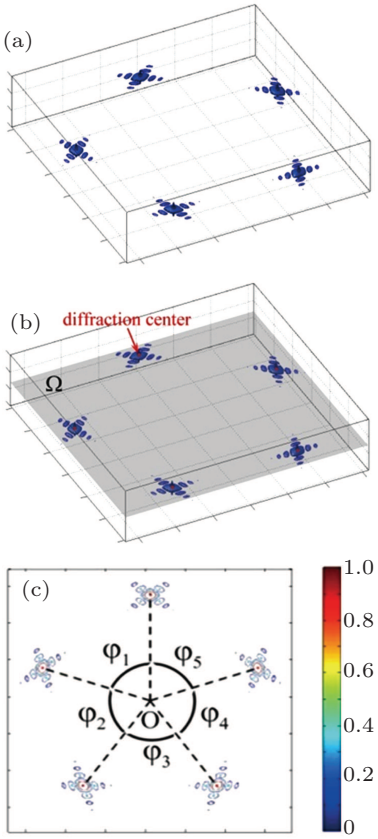


Fig. A3. (a) The simulated reciprocal volume containing (112) reflections diffracted from a star-shaped B_4C FTNW. (b) By finding the intensity maxima of five (112) reflections, the position of their diffraction centers can be identified. Then the plane passing through the five (112) reflection centers can be defined, here named as Ω. (c) In the Ω plane, finding the point O which has equal distances to the five diffraction centers. This point can be regarded as the projection of the twinning axis on the Ω plane. Then the angles φ_1, φ_2, φ_3, φ_4, and φ_5 can be measured. They are corresponding to the dihedral angles between the adjacent twin planes.

Experimental tilting series of electron diffraction patterns of the B_4C FTNW with diameter of 92-nm acquired on a JEOL JEM-2010 is shown in Fig. A4.

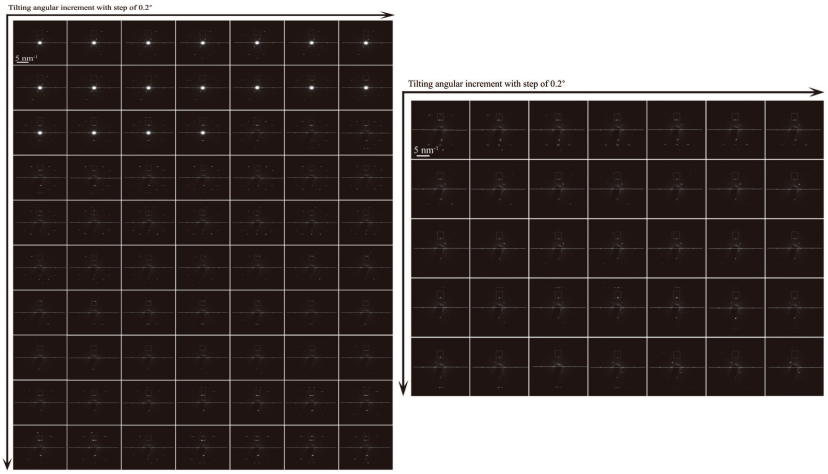


Fig. A4. The tilting axis is along the horizontal axis. The diffraction spots in the invariant line marked by white line in each diffraction pattern were used for the alignment of the tilting series. The areas marked by red rectangles were used for the 3D intensity reconstruction of (112) and (113) reflections as shown in Fig. 4(b).

Experimental tilting series of electron diffraction patterns of the Ag FTNW with diameter of 55 nm acquired on an FEI Technai F20 in shown in Fig. A5. The high resolution transmission electron microscope (HRTEM) images of two cross sections of the Ag FTNWs prepared by focused ion beams are shown in Fig. A6.

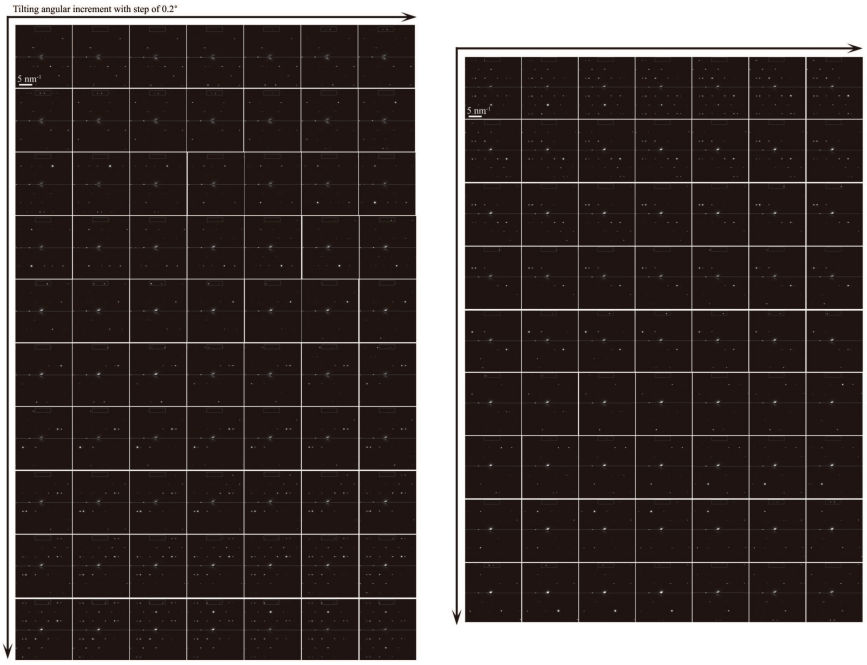


Fig. A5. The tilting axis is along the horizontal axis. The diffraction spots in the invariant line marked by white line in each diffraction pattern were used for the alignment of the tilting series. The areas marked by red rectangles were used for the 3D intensity reconstruction of (331) and reflections as shown in Fig. 7(b).

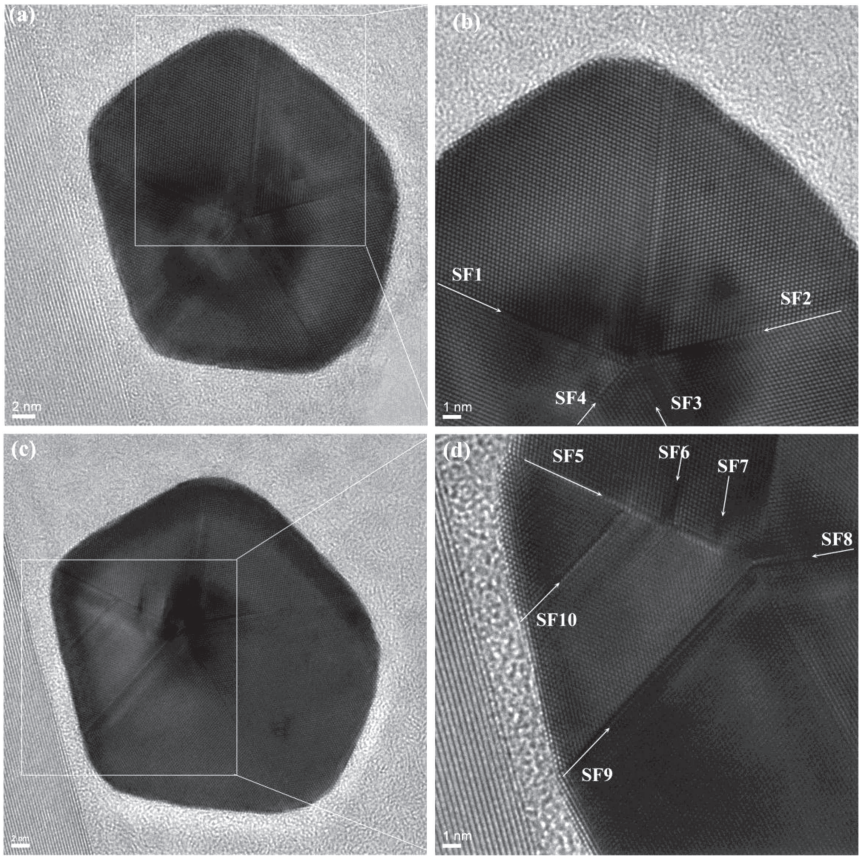


Fig. A6. (a) and (c) HRTEM images of two cross-sections of the Ag FTNWs prepared by focused ion beams (FIB). Panels (b) and (d) are the magnified images indicated by white square in panels (a) and (c), respectively. The stacking fault layers (SF1∼SF10) are indicated by white arrows. In panel (b), the four stacking fault layers, SF1, SF2, SF3, and SF4, are localized next to the twin planes. In panel (d), the stacking fault layers, SF5, SF8, and SF9, are also nearby their corresponding twin planes. The distances of the SF6, SF7, and SF10 to their parallel twin planes are about 2 nm, 4 nm, and 7 nm, respectively.

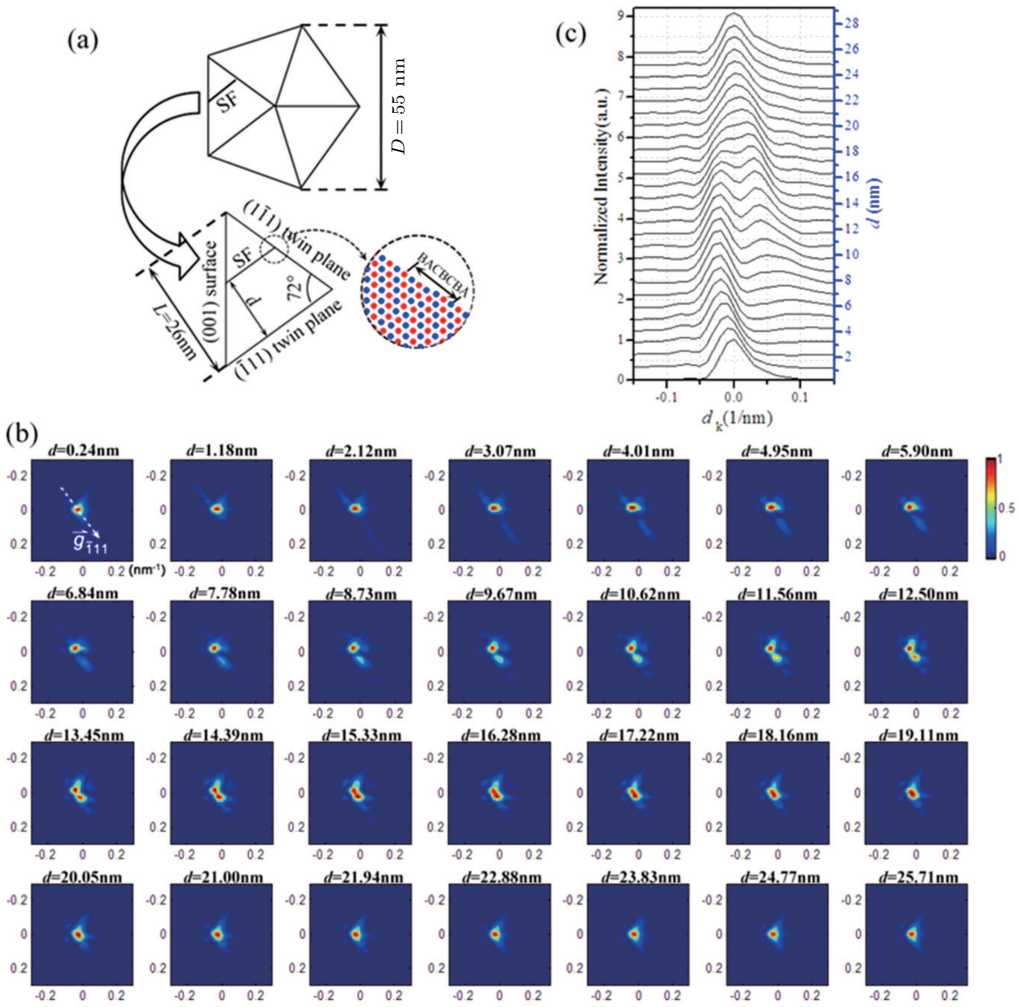


Fig. A7. (a) Cross-sectional structural model of a Ag single crystalline segment with disclination core and a single layer of stacking fault parallel to $(\bar{1}11)$ twin plane. The stacking fault layer changes the regular close packing of "$\cdots$ABCABC$\cdots$" to the packing sequence of "$\cdots$ABCBCABC$\cdots$". The distance between the stacking fault layer and its parallel twin plane is indicated by d. According to the structural model shown in panel (a), the kinematically simulated 2D intensity maps of (331) reflection perpendicular to the [110] twinning axis are shown in panel (b). (c) The series of $\boldsymbol{g}_{\bar{1}11}$ line-profile curves vertically aligned according to d value (*i.e.*, the distance of the stacking fault layer to its parallel twin plane).

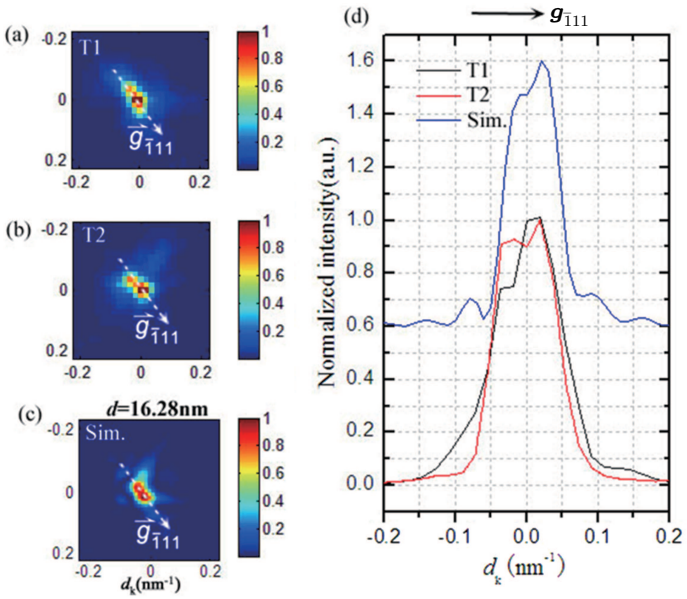


Fig. A8. Panels (a) and (b) are the (331) intensity distribution of T1 and T2 segments extracted from Fig. 8(a), respectively. (c) The kinematic simulation result of (331) intensity distribution in the plane perpendicular to the [110] twin axis according to the structural model (Sim.) with disclination core and a single layer of stacking fault parallel to the twin plane. In this structural model, the distance between the stacking fault layer and the twin plane is 16.28 nm. (d) The intensity line profiles along the $\boldsymbol{g}_{(\bar{1}11)}$ directions indicated by white dashed lines in panels (a), (b), and (c), respectively. For comparison, the simulated $\boldsymbol{g}_{(\bar{1}11)}$ line profile (Sim.) is vertically shifted.

References

[1] Hofmeister H 2004 *Encyclopedia of Nanoscience and Nanotechnology*, Nalwa H S ed. (American Scientific Publishers) pp. 431–452
[2] Liu S, Wang X Z, Tao H, Li T, Qi L, Xu Z, Fu X Z and Luo J L 2018 *Nano Energy* **45** 456
[3] Yu R, Wu H, Wang J D and Zhu J 2017 *ACS Appl. Mater. Interf.* **9** 4253
[4] Fu X, Jiang J, Liu C and Yuan J 2009 *Nanotechnology* **20** 365707
[5] Jiang J, Cao M H, Sun Y K, Wu P W and Yuan J 2006 *Appl. Phys. Lett.* **88** 163107
[6] Gryaznov V G, Heydenreich J, Kaprelov A M, Nepijko S A, Romanov A E and Urban J 1999 *Cryst. Res. Technol.* **34** 1091
[7] Wu B, Heidelberg A, Boland J J, Sader J E, Sun X and Li Y 2006 *Nano Lett.* **6** 468
[8] Zhu Y, Qin Q, Xu F, Fan F, Ding Y, Zhang T, J Wiley B and Wang Z 2012 *Phys. Rev. B* **85** 045443
[9] Pietrobon B, McEachran M and Kitaev V 2009 *ACS Nano* **3** 21
[10] Bian T, Zhang H, Jiang Y, Jin C, Wu J, Yang H and Yang D 2015 *Nano Lett.* **15** 7808
[11] De Wit R 1972 *J. Phys. C: Solid State Phys.* **5** 529
[12] Niekiel F, Bitzek E and Spiecker E 2014 *ACS Nano* **8** 1629
[13] Johnson C L, Snoeck E, Ezcurdia M, Rodriguez-Gonzalez B, Pastoriza-Santos I, Liz-Marzan L M and Hytch M J 2008 *Nat. Mater.* **7** 120
[14] Fu X, Jiang J, Zhang W and Yuan J 2008 *Appl. Phys. Lett.* **93** 043101
[15] Zhang W, Liu Y, Cao R, Li Z, Zhang Y, Tang Y and Fan K 2008 *J. Am. Chem. Soc.* **130** 15581
[16] Song M, Wu Z, Lu N and Li D 2019 *Chem. Mater.* **31** 842
[17] Chen H Y, Gao Y, Yu H C, Zhang H R, Liu L B, Shi Y G, Tian H F, Xie S S and Li J Q 2004 *Micron* **35** 469
[18] Fu X and Yuan J 2017 *Sci. Rep.* **7** 6206
[19] Kim J W, Ulvestad A, Manna S, Harder R, Fullerton E E and Shpyrko O G 2017 *Nanoscale* **9** 13153
[20] Zhu L, Shen X, Zeng Z, Wang H, Zhang H and Chen H 2012 *ACS Nano* **6** 6033
[21] Fu X and Yuan J 2013 *Nanoscale* **5** 9067
[22] Marks L D 1994 *Rep. Prog. Phys.* **57** 603
[23] Iijima S 1987 *Jpn. J. Appl. Phys.* **26** 365
[24] Pei Y T and De Hosson J T M 2001 *Acta Mater.* **49** 561
[25] Midgley P A and Dunin-Borkowski R E 2009 *Nat. Mater.* **8** 271
[26] Xia Y, Xiong Y, Lim B and Skrabalak S E 2009 *Angew. Chem. Int. Ed.* **48** 60
[27] Schmidt V, Wittemann J V, Senz S and Goesele U 2009 *Adv. Mater.* **21** 2681
[28] Allen J E, Hemesath E R, Perea D E, Lensch-Falk J L, Li Z Y, Yin F, Gass M H, Wang P, Bleloch A L and Palmer R E 2008 *Nat. Nanotechnol.* **3** 168
[29] Xing Y, Yu D, Xi Z and Xue Z 2002 *Chin. Phys.* **11** 1047
[30] Fu X and Yuan J 2014 *J. Phys.: Conf. Ser.* **522** 012064
[31] Fu X and Yuan J 2011 *J. Chin. Electron. Microsc. Soc.* **30** 439
[32] Sun Y, Ren Y, Liu Y, Wen J, Okasinski J S and Miller D J 2012 *Nat. Commun.* **3** 971
[33] Zhou Y and Fichthorn K A 2014 *J. Phys. Chem. C* **118** 18746
[34] McCarthy E K, Bellew A T, Sader J E and Boland J J 2014 *Nat. Commun.* **5** 4336
[35] Dodd S P, Saunders G A and James B 2002 *J. Mater. Sci.* **37** 2731
[36] Tao X, Dong L, Wang X, Zhang W, Nelson B J and Li X 2010 *Adv. Mater.* **22** 2055
[37] Yu Z Y, Fu X and Zhu J 2011 *Sci. Chin. (Technol. Sci.)* **54** 2119
[38] Ashbee K H G 1971 *Acta Metall.* **19** 1079
[39] Murr L E 1975 *Interfacial phenomena in metals and alloys* (Addison-Wesley Educational Publishers Inc.)
[40] Meyer R and Lewis L J 2002 *Phys. Rev. B* **66** 052106
[41] Narayanan S, Cheng G, Zeng Z, Zhu Y and Zhu T 2015 *Nano Lett.* **15** 4037
[42] Qin Q, Yin S, Cheng G, Li X, Chang T H, Richter G, Zhu Y and Gao H 2015 *Nat. Commun.* **6** 5983
[43] Patala S, Marks L D and Cruz M O D L 2013 *J. Phys. Chem. C* **117** 1485